

# Dust in brown dwarfs and extra-solar planets

## II. Cloud formation for cosmologically evolving abundances

S. Witte<sup>1</sup>, Ch. Helling<sup>2</sup>, and P. H. Hauschildt<sup>1</sup>

<sup>1</sup> Hamburger Sternwarte, Gojenbergsweg 112, 21029 Hamburg, Germany  
e-mail: switte@hs.uni-hamburg.de

<sup>2</sup> SUPA, School of Physics and Astronomy, University of St. Andrews, North Haugh, St. Andrews KY16 9SS, UK

Received ?? / Accepted ??

### ABSTRACT

**Aims.** Substellar objects have extremely long life-spans. The cosmological consequence for older objects are low abundances of heavy elements, which results in a wide distribution of objects over metallicity, hence over age. Within their cool atmosphere, dust clouds become a dominant feature, affecting the opacity and the remaining gas phase abundance of heavy elements. We investigate the influence of the stellar metallicity on the dust formation in substellar atmospheres and on the dust cloud structure and its feedback on the atmosphere. This work has implications for the general question of star formation and of dust formation in the early universe.

**Methods.** We utilize numerical simulations in which we solve a set of moment equations in order to determine the quasi-static dust cloud structure (DRIFT). These equations model the nucleation, the kinetic growth of composite particles, their evaporation and the gravitational settling as a stationary dust formation process. Element conservation equations augment this system of equations including the element replenishment by convective overshooting. The integration with an atmosphere code (PHOENIX) allows to determine a consistent  $(T, p, v_{\text{conv}})$ -structure ( $T$  - local temperature,  $p$  - local pressure,  $v_{\text{conv}}$  - convective velocity), and, hence, also to calculate synthetic spectra.

**Results.** A grid of DRIFT-PHOENIX model atmospheres was calculated for a wide range of metallicity,  $[M/H] \in [+0.5, -0.0, -0.5, \dots, -6.0]$ , to allow for a systematic study of atmospheric cloud structures throughout the evolution of the universe. We find dust clouds in even the most metal-poor ( $[M/H] = -6.0$ ) atmosphere of brown dwarfs. Only the most massive among the youngest brown dwarfs and giant gas planets can resist dust formation. For very low heavy element abundances, a temperature inversion develops which has a drastic impact on the dust cloud structure.

**Conclusions.** The combination of metal depletion by dust formation and the uncertainty of interior element abundances makes the modeling of substellar atmospheres an intricate problem in particular for old substellar objects. We further show that the dust-to-gas ratio does *not* scale linearly with the object's  $[M/H]$  for a given effective temperature. The mean grain sizes and the composition of the grains change depending on  $[M/H]$  which influences the dust opacity that determines radiative heating and cooling as well as the spectral appearance.

**Key words.** astrochemistry - Methods: numerical - Stars: atmospheres - Stars: low-mass, brown dwarfs

### 1. Introduction

Condensation of supersaturated gas species becomes a major issue in ultracool atmospheres, i.e. that of brown dwarfs and giant planets. The formation of solid dust particles or liquid droplets depletes the gas phase of elements and, hence, strongly affects the chemical composition of the remaining gas phase. In addition, the forming dust particles represent an important opacity source, which ultimately results in a significant backwarming and an increased gas temperature compared to a cloud-free atmosphere (Tsuji et al. 1996a).

Besides the dust formation induced element deficiency, the substellar object can already have formed from a metal-poor gas, hence, being intrinsically metal-deficient. The first generation of stars was comprised of extremely massive objects. These stars were responsible for a strong metal enrichment of the interstellar medium, from which new stars formed. The corresponding enrichment of the ISM with more and more heavy elements had an important impact on the star formation, as it brought about the collapse of much smaller cloud fragments (Smith & Sigurdsson 2007). Hence, succeeding star generations contained growing numbers of smaller objects. The debate about the lower mass

limit for stellar formation is still not settled. For solar abundances, simulations by Whitworth & Stamatellos (2006) predict a limit for the mass of collapsing gas clouds as low as 0.001 to 0.004  $M_{\odot}$ . Results by e.g. Boss (2001) and Bate (2005) fall in a similar mass regime. Observations by Greaves et al. (2003) and Greaves (2005) present evidence for the formation of objects with masses below the deuterium burning limit via a gravitational collapsing molecular cloud fragment. The presence of discs around 8-10  $M_{\text{Jup}}$ -objects (Natta et al. (2002), Luhman et al. (2005), Scholz & Jayawardhana (2008)) is also evidence for the formation of such low-mass objects via gravitational cloud collapse. According to Omukai (2008) and Clark et al. (2008) subsolar mass objects may already have formed at  $[M/H] \geq -6.0$ , though heating effects may have obstructed the collapse of low mass gas clouds and depopulated the range between  $[M/H] = -4.0$  and  $-5.0$ . Jappsen et al. (2009) note that the transition of the early universe IMF to the present day IMF at around  $[M/H] = 10^{-6} - 10^{-5}$  seem to be determined by dust cooling which in turn is determined by the grain size distribution and composition of the dust forming at these low metallicities. Those extreme metallicities can be attributed to a much earlier state of the universe, when the continuously run-

ning heavy element enrichment of the interstellar medium by nucleosynthesis inside massive stars and supernovae had not progressed as far as today. The implication is a wide distribution of objects over the metallicity range. However, all but the lowest mass objects of high age, i.e. of extremely low metallicities, have already exceeded their life-span as main-sequence stars. Therefore, only ultracool stars and substellar objects remain from those earlier stages of the universe. Hence, substellar spectra need to be characterised not only by effective temperature,  $T_{\text{eff}}$ , and surface gravity,  $\log(g)$ , but also by the interior, well-mixed element abundances as relic of the conditions at their formation.

The presence of dust in ultracool dwarf and substellar atmospheres has been suggested first by Lunine et al. (1986) and was noticed by Jones & Tsuji (1997). First observational evidence for convective activity in substellar objects was found by Noll et al. (1997) and Oppenheimer et al. (1998). By then, the first brown dwarfs had just been discovered by Rebolo et al. (1995) and Nakajima et al. (1995). The observation of metal-poor ultracool stars in the galactic halo (e.g., Christlieb (2006)) led to the classification into dwarfs, subdwarfs and extreme subdwarfs (Gizis 1997). A later revision of this system was done by Lépine et al. (2007), introducing the even more metal-poor ultra-subdwarfs class. The first substellar subdwarfs were discovered by Burgasser et al. (2003) and Burgasser (2004).

As the importance of dust clouds in late-M-, L- and T-type dwarf atmospheres had been recognised, models were developed to help to understand these objects. Initially, the clouds were parameterised by a constant grain size (Tsuji et al. 1996b; Burrows et al. 2006), later time-scale arguments were applied (Allard et al. 2001), or grain size distributions guided by Earth-observations were used (Cooper et al. 2003; Ackerman & Marley 2001). All these models apply complete ( $S = 1$ ) or almost ( $S = 1.01$ ) phase-equilibrium. A detailed comparison study of current dust models was made by Helling et al. (2008a).

We consider a stationary dust formation process, where seeds form high up in the atmosphere from a highly supersaturated gas, grow to macroscopic particles of around a  $\mu\text{m}$  in size, gravitationally settle into deeper layers and eventually evaporate as the local temperature becomes too high for thermal stability (Woitke & Helling 2003). The basic idea is that a “dirty” solid mantle will grow on top of the seed particles. This dirty mantle is assumed to be composed of numerous small islands of different pure condensates. The formation of islands is supported by experiments in solid state physics (Ledieu et al. 2005) and by observations of coated terrestrial dust particles (Levin et al. 1996; Korhonen et al. 2003).

## 2. Method

We make use of the DRIFT-PHOENIX model atmosphere code, introduced by Dehn (2007) and Helling et al. (2008b). The general-purpose model atmosphere code PHOENIX (Hauschildt & Baron 1999; Baron et al. 2003) solves the gas-phase equation of state, provides the atmosphere structure to DRIFT, determines the gas opacities and solves the radiative transfer. The DRIFT code by Helling, Woitke, & Thi (2008c) is included as a module in order to calculate the dust clouds, which feed back on both the thermodynamical structures and the radiation field. An iteration of this method allows the determination of the atmosphere and dust cloud properties and yields the corresponding synthetic spectra. For a given atmosphere structure ( $T, p, v_{\text{conv}}$ ), provided by PHOENIX, the phase non-

equilibrium dust formation with subsequent precipitation and element replenishment by convective overshooting is calculated by DRIFT. The opacities of the composite dust particles, which are required for the radiative transfer, are determined by using effective medium theory (Bruggeman 1935) and Mie theory (Mie 1908; Wolf & Voshchinnikov 2004). All dust species are included as opacity source since our dust grains are made of a mixtures of these compounds.

### 2.1. Gas-phase chemistry

The chemistry in PHOENIX considers the 40 most important elements in several ionization states and 47 molecule species. Though larger chemical systems are possible, the results differ only marginally (Dehn 2007). For the solar element abundances, defining  $[M/H]=0.0$  in our models, we utilize data from Grevesse et al. (1992). We are aware that the elemental composition of brown dwarfs and planets is dependent on the initial composition of the gas cloud they formed from, which itself depends critically on the internal physics of its local preceding star generations, like, e.g., the efficiency of the various burning cycles and the resulting amount of elements. Especially for extremely low metallicities, the element abundance pattern is completely different to the one we know from the solar environment (e.g., Frebel et al. (2005), Campbell & Lattanzio (2008)). However, we neglect variations of the individual element abundances relative to each other and their impact on metallicity model sequences for the sake of simplicity and determine the varied metallicity values by a single scaling-factor. These values are varied according to the metallicity under consideration such that  $[M/H]=+0.5 \dots -6.0$ .

The PHOENIX chemistry utilizes the altitude-dependent gas phase abundances  $\epsilon_i$  of the elements Mg, Si, Ti, O, Fe, and Al provided by DRIFT, i.e., it takes into account those element abundances which have been altered throughout the atmosphere by depletion (nucleation, dust growth), enrichment (evaporation) and redistribution (precipitation, convective overshooting). In the DRIFT-module, we calculate the number densities of all gaseous species, including the number density of the key reactant  $n_r^{\text{key}}$  as described in Woitke & Helling (2004) according to pressure, temperature and the calculated depth-dependent element abundances  $\epsilon_i$  in chemical equilibrium. For the well-mixed, deep element abundances  $\epsilon_i^0$  we use the scaled solar abundances of the model input. For those elements that are not included in the DRIFT chemistry calculations, we set  $\epsilon_i = \epsilon_i^0$ .

## 3. Growth reactions

### 3.1. Dust seed formation

The nucleation rate  $J_*$  is calculated for  $(\text{TiO}_2)_N$ -clusters according to Eq. (34) in Helling & Woitke (2006), applying the modified classical nucleation theory of Gail et al. (1984). We use the value of the surface tension  $\sigma$  fitted to small cluster data by Jeong et al. (2000) as outlined in Woitke & Helling (2004).

### 3.2. Dust growth/evaporation & refractive indices

The dust growth of dirty particles is modelled according to Woitke & Helling (2003), Helling & Woitke (2006) and Helling et al. (2008c). However, compared to Helling et al. (2008c), we consider only the 7 most important solids ( $\text{TiO}_2[\text{s}]$ ,  $\text{Al}_2\text{O}_3[\text{s}]$ ,  $\text{Fe}[\text{s}]$ ,  $\text{SiO}_2[\text{s}]$ ,  $\text{MgO}[\text{s}]$ ,  $\text{MgSiO}_3[\text{s}]$ ,  $\text{Mg}_2\text{SiO}_4[\text{s}]$ )

Solid s	Surface reaction r	Key species
TiO <sub>2</sub> [s] rutile (1) (A)	TiO <sub>2</sub> → TiO <sub>2</sub> [s] Ti + 2 H <sub>2</sub> O → TiO <sub>2</sub> [s] + 2 H <sub>2</sub> TiO + H <sub>2</sub> O → TiO <sub>2</sub> [s] + H <sub>2</sub> TiS + 2 H <sub>2</sub> O → TiO <sub>2</sub> [s] + H <sub>2</sub> S + H <sub>2</sub>	TiO <sub>2</sub> Ti TiO TiS
SiO <sub>2</sub> [s] silica (3)(B)	SiO <sub>2</sub> → SiO <sub>2</sub> [s] SiO + H <sub>2</sub> O → SiO <sub>2</sub> [s] + H <sub>2</sub> SiS + 2 H <sub>2</sub> O → SiO <sub>2</sub> [s] + H <sub>2</sub> S + H <sub>2</sub>	SiO <sub>2</sub> SiO SiS
Fe[s] solid iron (1) (B)	Fe → Fe[s] FeO + H <sub>2</sub> → Fe[s] + H <sub>2</sub> O FeS + H <sub>2</sub> → Fe[s] + H <sub>2</sub> S Fe(OH) <sub>2</sub> + H <sub>2</sub> → Fe[s] + 2 H <sub>2</sub> O	Fe FeO FeS Fe(OH) <sub>2</sub>
MgO[s] periclase (3) (B)	MgO → MgO[s] Mg + H <sub>2</sub> O → MgO[s] + H <sub>2</sub> 2 MgOH → 2 MgO[s] + H <sub>2</sub> Mg(OH) <sub>2</sub> → MgO[s] + H <sub>2</sub> O	MgO Mg ½MgOH Mg(OH) <sub>2</sub>
MgSiO <sub>3</sub> [s] enstatite (3) (C)	Mg + SiO + 2 H <sub>2</sub> O → MgSiO <sub>3</sub> [s] + H <sub>2</sub> Mg + SiS + 3 H <sub>2</sub> O → MgSiO <sub>3</sub> [s] + H <sub>2</sub> S + 2 H <sub>2</sub> 2 MgOH + 2 SiO + 2 H <sub>2</sub> O → 2 MgSiO <sub>3</sub> [s] + 3 H <sub>2</sub> 2 MgOH + 2 SiS + 2 H <sub>2</sub> O → 2 MgSiO <sub>3</sub> [s] + 2 H <sub>2</sub> S + 2 H <sub>2</sub> Mg(OH) <sub>2</sub> + SiO → 2 MgSiO <sub>3</sub> [s] + H <sub>2</sub> Mg(OH) <sub>2</sub> + SiS + H <sub>2</sub> O → MgSiO <sub>3</sub> [s] + H <sub>2</sub> S + H <sub>2</sub>	min(Mg, SiO) min(Mg, SiS) min(½MgOH, ½SiO) min(½MgOH, ½SiS) min(Mg(OH) <sub>2</sub> , SiO) min(Mg(OH) <sub>2</sub> , SiS)
Mg <sub>2</sub> SiO <sub>4</sub> [s] forsterite (3) (C)	2 Mg + SiO + 3 H <sub>2</sub> O → Mg <sub>2</sub> SiO <sub>4</sub> [s] + 3 H <sub>2</sub> 2 MgOH + SiO + H <sub>2</sub> O → Mg <sub>2</sub> SiO <sub>4</sub> [s] + 2 H <sub>2</sub> 2 Mg(OH) <sub>2</sub> + SiO → Mg <sub>2</sub> SiO <sub>4</sub> [s] + H <sub>2</sub> O + H <sub>2</sub> 2 Mg + SiS + 4 H <sub>2</sub> O → Mg <sub>2</sub> SiO <sub>4</sub> [s] + H <sub>2</sub> S + 3 H <sub>2</sub> 2 MgOH + SiS + 2 H <sub>2</sub> O → Mg <sub>2</sub> SiO <sub>4</sub> [s] + H <sub>2</sub> S + 2 H <sub>2</sub> 2 Mg(OH) <sub>2</sub> + SiS → Mg <sub>2</sub> SiO <sub>4</sub> [s] + H <sub>2</sub> + H <sub>2</sub> S	min(½Mg, SiO) min(½MgOH, SiO) min(½Mg(OH) <sub>2</sub> , SiO) min(½Mg, SiS) min(½MgOH, SiS) min(½Mg(OH) <sub>2</sub> , SiS)
Al <sub>2</sub> O <sub>3</sub> [s] alumina (3) (D)	2 AlOH + H <sub>2</sub> O → Al <sub>2</sub> O <sub>3</sub> [s] + 2 H <sub>2</sub> 2 AlH + 3 H <sub>2</sub> O → Al <sub>2</sub> O <sub>3</sub> [s] + 4 H <sub>2</sub> Al <sub>2</sub> O + 2 H <sub>2</sub> O → Al <sub>2</sub> O <sub>3</sub> [s] + 2 H <sub>2</sub> 2 AlS + 3 H <sub>2</sub> O → Al <sub>2</sub> O <sub>3</sub> [s] + 2 H <sub>2</sub> S + H <sub>2</sub> 2 AlO <sub>2</sub> H → Al <sub>2</sub> O <sub>3</sub> [s] + H <sub>2</sub> O	½AlOH ½AlH Al <sub>2</sub> O ½AlS ½AlO <sub>2</sub> H

**Table 1.** Chemical surface reactions  $r$  assumed to form the solid materials  $s$ . The efficiency of the reaction is limited by the collision rate of the key species. The notation  $\frac{1}{2}$  in the r.h.s. column means that only every second collision (and sticking) event initiates one reaction. Data sources for the supersaturation ratios (and saturation vapour pressures): (1) Helling & Woitke (2006); (2) Nuth & Ferguson (2006); (3) Sharp & Huebner (1990). Data sources for the pure solid refractive indices: (A) Posch (2008); (B) Palik (1985, 1991); (C) Jäger et al. (2003); (D) Palik (1991), Begemann et al. (1997).

made of 6 different elements for which we solve the resulting, stiff system of 15 ( $3 \times \text{Eq.}(8)$ ,  $7 \times \text{Eq.}(9)$ ,  $5 \times \text{Eq.}(10)$  in Helling et al. (2008c)) dust moment and element conservation equations.

The 7 considered solids are formed by 32 chemical surface reaction (see Table 1) in phase-non-equilibrium to calculate the formation and composition of the dirty grains. Our selection is guided by the most stable condensates which yet have simple stoichiometric ratios, ensuring that these solids can be easily built up from the gas phase (for more details see Sect. 3.4. in Helling, Woitke, & Thi (2008c)). Note that we consider dust formation by gas-solid reactions only and omit solid-solid reactions and lattice rearrangements inside the grains in our model (see Helling & Rietmeijer (2009) regarding lattice rearrangements in clouds in substellar atmospheres). Table 1 also contains the solid refractive index data used in the Mie calculations.

### 3.3. Element replenishment

A truly static atmosphere would not contain any dust (Woitke & Helling 2004). Therefore, we include mixing by convection and overshooting by assuming an exponential decrease of the mass exchange frequency in the radiative zone (Eq. 9 in (Woitke & Helling 2004) with  $\beta = 2.2$  and  $\tau_{\text{mix}}^{\text{min}} = 2/(H_p v_{\text{conv}})$ ), which serves to replenish the upper atmospheres and keeps the cycle of dust formation running.

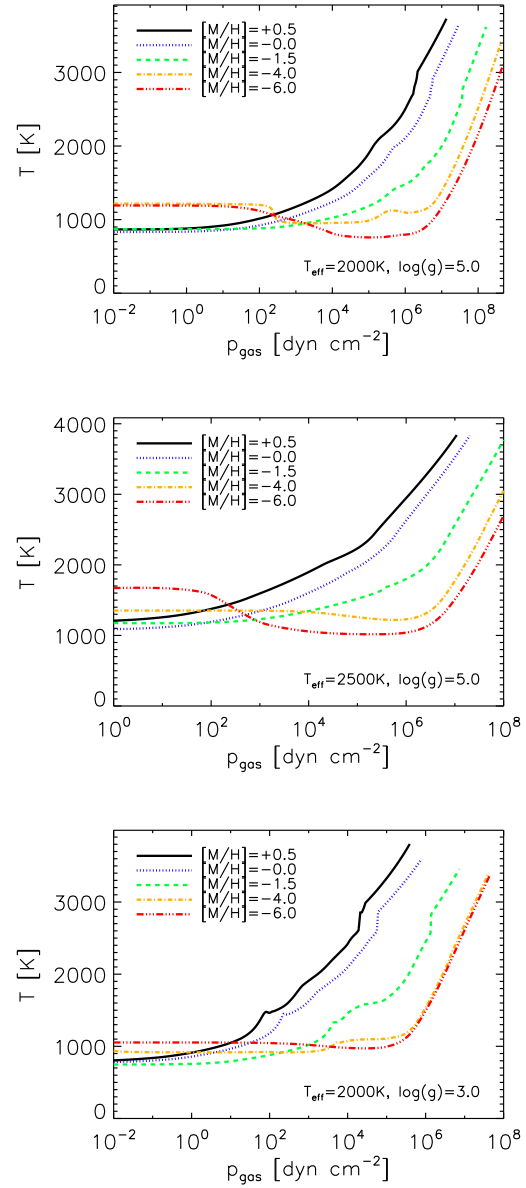


**Fig. 1.**  $(T, p)$ -structures for three model sequences of varying metallicity  $[M/H]$ : **Top:**  $T_{\text{eff}}=2000\text{K}$ ,  $\log(g)=5.0$ ; **Center:**  $T_{\text{eff}}=2500\text{K}$ ,  $\log(g)=5.0$ ; **Bottom:**  $T_{\text{eff}}=2000\text{K}$ ,  $\log(g)=3.0$

### 3.4. Grain size distribution function

The dust opacity calculations with effective medium theory and Mie theory require the grain size distribution function  $f(a)$  [ $\text{cm}^{-4}$ ] at every depth in the atmosphere, where  $a$  [cm] is the grain radius. This function is not a direct result of the dust moment method. Only the total dust particle number density  $n_d = \rho L_0$  and the mean particle size  $\langle a \rangle = \sqrt[3]{3/(4\pi)} L_1/L_0$  are direct results that have been used in Helling & Woitke (2006). In this paper, we reconstruct  $f(a)$  from the calculated dust moments  $L_j$  ( $j = 1 \dots 4$ ) in an approximate way as described in Appendix A in Helling, Woitke, & Thi (2008c). In this paper, we apply the double delta-peaked size distribution function  $f(a) = N_1 \delta(a - a_1) + N_2 \delta(a - a_2)$  where  $\delta$  is the Dirac-function,  $N_1, N_2$  [ $\text{cm}^{-3}$ ] are two dust particle densities and  $a_1, a_2$  [cm] are the two corresponding particle radii.

## 4. Results: The model grid

In this section we will describe the influence of metallicity on the model atmospheres and the dust cloud. This will be done for three showcase model sequences to exemplarily cover the parameter space for effective temperature and surface gravity which covers brown dwarfs and giant gas planets. We think that such a detailed demonstration of our dust model results is necessary as dust cloud model for brown dwarfs differ considerably with respect to dust properties (Helling et al. 2008a).

The sequences are calculated for:

$$T_{\text{eff}} = 2000\text{K} \text{ and } \log(g)=5.0,$$

$$T_{\text{eff}} = 2500\text{K} \text{ and } \log(g)=5.0$$

$$T_{\text{eff}} = 2000\text{K} \text{ and } \log(g)=3.0,$$

covering the metallicity values  $[M/H] \in [+0.5, -0.0, -0.5, \dots, -6.0]$ . In the following, we will concentrate on only  $[M/H] \in [+0.5, -0.0, -1.5, -4.0, -6.0]$ .

### 4.1. Metallicity-dependent temperature-pressure structures

At first, we will take a look how the temperature-pressure structures are affected by the metallicity (Fig. 1). As one might expect, the local temperature decreases with  $[M/H]$  for a fixed pressure, due to the smaller gas opacities. However, the outer atmospheres of the low  $[M/H]$  models feature a strong temperature inversion. It is caused by a tilt in the chemical equilibrium, favouring the formation of methane instead of carbon monoxide, which frees up oxygen for the formation of water and metal oxides (e.g., Allard & Hauschildt (1995)). The inversion becomes stronger for higher effective temperatures and higher surface gravities for a given  $[M/H]$ -value.

Figure 1 demonstrates that the local pressure increases for a given local temperature with decreasing metallicity but with increasing gravity. This relative pressure increase strengthens the contribution of strongly pressure-dependent gas-phase opacity sources like the collision induced absorption but also the contribution of the pressure-broadened alkali lines. Fortney et al. (2008) present similar findings for cooler substellar objects with  $T_{\text{eff}} \lesssim 1400\text{K}$ . Hence, the effect of increasing pressure with decreasing metal content holds across the whole substellar range of  $T_{\text{eff}}$ . Therefore, clouds in giant planets but also in low-metallicity substellar objects form at even lower gas temperatures at a comparable pressure (see Sect. 4.3).

The dust clouds represent a strong opacity source. Therefore, the backwarming caused by the dust particles strongly increases the local gas temperature at and below the cloud location. Hence, dense cloud layers coincide with a strong inward temperature gradient. Especially the high  $[M/H]$  models feature two bends around 1500K and 2000K. The drop of the local temperature gradient is caused by the starting evaporation of the solid species. The lower temperature bend is attributed to the evaporation of the silicate species ( $\text{MgO}[\text{s}]$ ,  $\text{SiO}_2[\text{s}]$ ,  $\text{MgSiO}_3[\text{s}]$ ,  $\text{Mg}_2\text{SiO}_4[\text{s}]$ ), while the second corresponds to evaporation of the thermally more stable species ( $\text{Fe}[\text{s}]$ ,  $\text{TiO}_2[\text{s}]$ ,  $\text{Al}_2\text{O}_3[\text{s}]$ ).

In the  $T_{\text{eff}}=2000\text{K}$  model for  $\log(g)=5.0$  and  $[M/H]=-4.0$ , there is a bump in the (T,p)-structure around  $6 \cdot 10^6 \text{ dyn cm}^{-2}$ . It already appears for  $[M/H]=-2.0$  and remains until  $[M/H]=-5.0$ . The origin is the superposition of two effects, namely the decreasing deep interior abundances and the decreasing depletion of the gas phase with the metallicity. This causes a locally higher absolute Ti abundance in the gas phase compared to atmospheres of even higher metallicities. The opacity by the re-

sulting increased amount of TiO is the reason for this feature in the (T,p)-structure.

### 4.2. Metallicity influence on the $(v_{\text{conv}}, p)$ -structure

Solar-metallicity models ( $[M/H]=0.0$ ) suggest that the dust cloud location and the convectively unstable zone are well separated. Even so, convection provides a mechanism for element replenishment of the upper atmosphere layer, which assures stationarity of the cloud formation process. The so-called convective overshooting is parameterised in DRIFT by a mixing-time scale (Woitke & Helling 2004) following the idea of momentum conservation of the convective mass elements (see Ludwig et al. (2002, 2006)) whose motion does not instantly end where the Schwarzschild criterion is no longer met, but decays slowly into the higher layers (Woitke & Helling 2004). A higher maximum convection velocity consequently yields a more efficient mixing into the upper layers.

Due to the vanishing local opacities with decreasing  $[M/H]$ , the radiative flux is less obstructed and, hence, the convective energy transport becomes less important. For this reason, the convection zone is shifted inwards to higher pressures and densities for decreasing metallicities. According to mixing length theory, the resulting mean convection velocity  $v_{\text{conv}}$  decreases, which results in a less efficient convective overshooting. Because of a weaker radiation field for decreasing effective temperatures and higher gas densities for increasing surface gravity, one finds a similar effect on the convective velocity and overshooting for these parameters.

Hence, the convective overshooting is more efficient in hot, low-gravity objects. An improved mixing consequently enables the dust cloud to persist into higher atmosphere layers. Hence, hot-Jupiters should have high-altitude clouds which supports what Richardson et al. (2007) and Pont et al. (2008) suggested for their observed giant gas planets.

### 4.3. Metallicity-dependent cloud structure

We study the influence of the stellar metallicity on the dust cloud structure to provide insight into possible diversities of cloud properties for substellar objects originating from different evolutionary states of the universe, i.e. for objects which have formed from interstellar gas clouds of different metal-enrichment.

Figure 2 contains the results including the  $(T, p)$ -structures for better comparison. Depicted are the number of dust particles forming per volume element and time, i.e. the nucleation rate  $J_* [\text{cm}^{-3}\text{s}^{-1}]$  (2<sup>nd</sup> panel), the net growth velocity  $\chi_{\text{net}} = \sum_s \chi^s [\text{cm s}^{-1}]$  (3<sup>rd</sup> panel; Eq. (7) in Helling et al. (2008c)), the mean grain size  $\langle a \rangle = \sqrt[3]{3/(4\pi)} L_1/L_0 [\text{cm}]$  (4<sup>th</sup> panel), and the equilibrium drift velocity  $\langle v_{\text{dr}} \rangle = \sqrt{\pi} g \rho_d(a) / (2\rho_{\text{CT}}) [\text{cm s}^{-1}]$  (5<sup>th</sup> panel), which is determined for gravitationally settling particles of mean size, retarded by friction for the case of free molecular flows (Woitke & Helling 2003).

#### 4.3.1. The general, high- $[M/H]$ cloud structure

As is shown in Fig. 2, all high metallicity models exhibit a typical cloud structure which was already shown in our previous publications. At the highest altitudes with its dust-poor depleted gas (compare Woitke & Helling (2004)), dust seeds form which are unable to grow perceptibly due to the extremely low densities at these altitudes. The mean grain size,  $\langle a \rangle$ , remains of the order of the seed particle size. Due to the low density, the num-

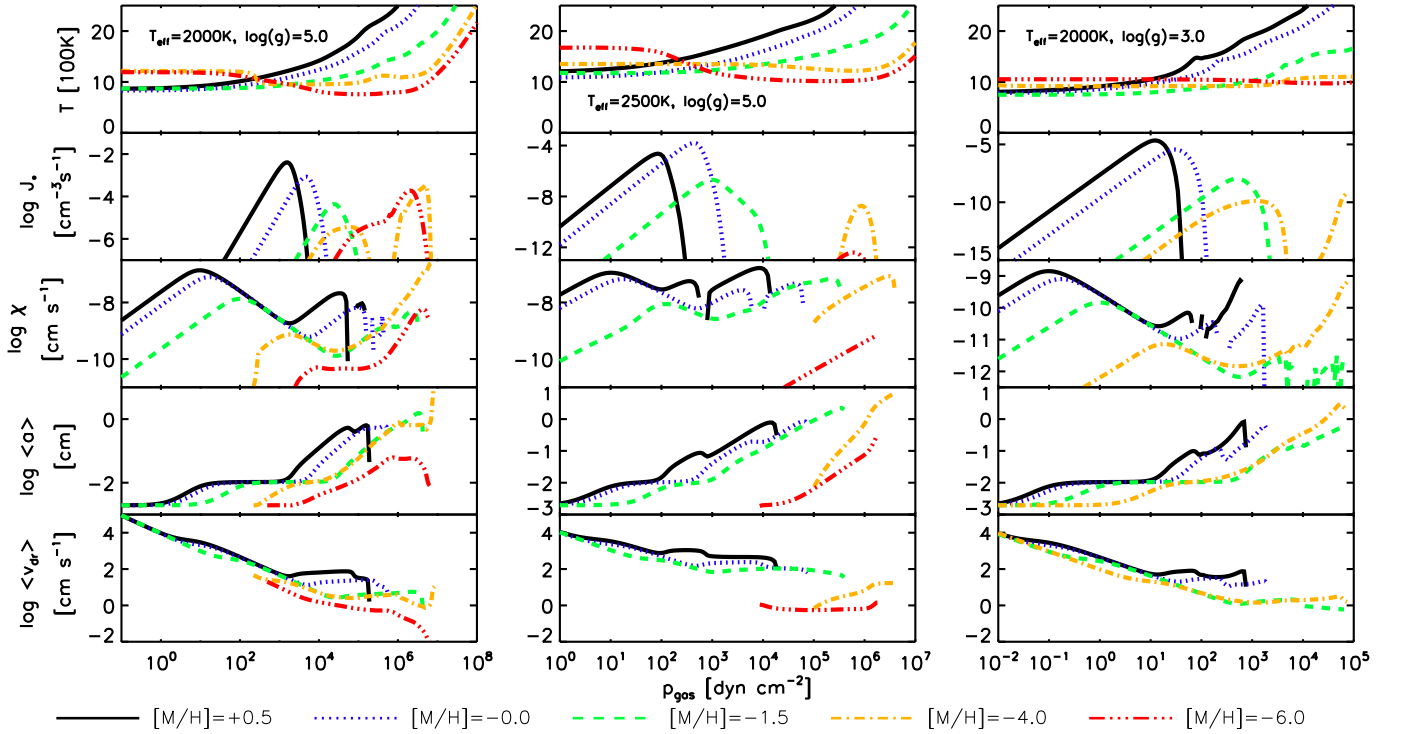


**Fig. 2.** Cloud structures for three model sequences of varying metallicity  $[M/H]$ . **Left:**  $T_{\text{eff}}=2000\text{K}$ ,  $\log(g)=5.0$ ; **Center:**  $T_{\text{eff}}=2500\text{K}$ ,  $\log(g)=5.0$ ; **Right:**  $T_{\text{eff}}=2000\text{K}$ ,  $\log(g)=3.0$ . **1<sup>st</sup> row:** local temperature  $T$  [K], **2<sup>nd</sup> row:** nucleation rate  $J_*$  [ $\text{cm}^{-3}\text{s}^{-1}$ ], **3<sup>rd</sup> row:** net growth velocity  $\chi_{\text{net}}$  [ $\text{cm s}^{-1}$ ], **4<sup>th</sup> row:** mean grain size  $\langle a \rangle$  [cm], **5<sup>th</sup> row:** mean drift velocity  $\langle v_{\text{dr}} \rangle$  [ $\text{cm s}^{-1}$ ].

ber of the dust particles remains very low (not shown), but the particles can settle very fast into deeper layer for the same reason. The net grain growth velocity,  $\chi_{\text{net}}$ , increases proportionally to the gas density, while the drift velocity,  $\langle v_{\text{dr}} \rangle$ , decreases. From a certain depth downward, the mean particle size increases from the initial size of the seeds. Together with the increasing nucleation rate, the dust growth starts to cause a steep drop of the local gas-phase element abundances with depth (compare Fig. 6). The consequence is that the growth velocity eventually decreases to a degree, that the particles settle too fast to sustain a perceptible growth of the mean grain radius at this low-pressure region. Gravitational settling does not influence the process of seed formation since nucleation proceeds much faster. However, the strong gas-phase depletion will impede the formation of more seeds as less material is available. As the precipitating particles drop into atmosphere layers which are closer to the edge of the convection zone, the convective upmixing becomes more efficient. The more efficient mixing results in a continuously increasing nucleation rate with depth as more material is available to form seed from. The gas-phase depletion by the exponential increase of the number of new seed particles compensates for the on-going growth of the grains. Hence, the mean grain radius remains constant, even though there is growth, which is strong enough to cause an exponentially decreasing element abundances, shown in Fig. 6. In this region, the dust cloud becomes optically thick enough to cause a perceptible backwarming of up to several hundred degrees (Fig. 1). As the local temperatures are increasing and the abundances are decreasing with depth, the nucleation rate reaches its apex and drops to zero very fast over the next few atmospheric layers. This also means, the particle production has reached its maximum. Hence, dust existing in deeper layers must have rained in from above. Therefore, changes in the number density of the dust particles in these deeper atmospheric layers

are caused by accumulation, drift and evaporation. Interestingly, the dust number density remains of the same order compared to the site of the nucleation maximum, but the grain size distribution changes dramatically.

The end of nucleation sparks a strong increase of the mean grain size. The frictional force caused by the high densities at these layers has strongly decreased the drift velocity. Thus, it takes the dust particles much longer to cross a given atmospheric layer. This allows the particles to capture more and more reactants from the gas phase, resulting in an even stronger growth. In turn, the mean grain radius causes an increase of the drift velocity. This is balanced by the increasing gas density, which is why we observe a plateau-like feature in the drift velocity (Fig. 2, lowest panel). The numerous  $\mu\text{m}$ -sized particles below the nucleation maximum cause a strong backwarming.

As soon as the evaporation of a certain species exceeds its growth, it is vanishing from the solid phase. This is accompanied by a decreasing and possibly even negative growth velocity. That is the reason for the observed kinks (Fig. 2) in the mean grain radius curves and all consequential kinks in other quantities like, e.g., the effective temperature, as mention in Sec. 4.1. As soon as the last solid species starts to evaporate, the dust cloud typically vanishes very fast with depth.

#### 4.3.2. The influence of metallicity on the cloud structure

The convective mixing becomes less efficient with decreasing  $[M/H]$  (Sec. 4.2). Thus, the dust clouds are located at higher gas pressures and densities for lower  $[M/H]$ . However, this is also caused by an additional factor, which is a temperature inversion in the outer atmosphere (Sec. 4.1, Fig. 1), developing for metallicities below  $[M/H]=-3.0$ . Within this inversion zone, the gas phase is no longer supersaturated for the lowest consid-

ered metallicities. Thus, no dust can form there and the typical structure of undisturbed dust clouds is lost. In these model atmospheres, the dust cloud is bottled up in a temperature “valley” between the inversion zone and the hotter inner atmosphere. This valley becomes more distinctive for increasing surface gravity, i.e., it will vanish for planet-like objects but persist within the coolest amongst the brown dwarfs (Fig. 1).

Depending on metallicity, the atmospheres can have one or two zones of efficient nucleation, i.e. two nucleation rate maxima  $J_*^{\max}$ . High-metallicity models show only the outer nucleation zone, as reported by Woitke & Helling (2003) and Helling, Woitke, & Thi (2008c). Very metal-deficient models ( $[M/H] < -4.0$ ) develop a very shallow outer nucleation zone and an additional inner zone of much more efficient seed formation. The outer nucleation zone is already indicative for a layer of haze. Nucleation takes place throughout the dust cloud for low metallicities in contrast to the higher metallicity models, where nucleation ceases in the middle of the cloud. Generally, the maximum nucleation rate is decreasing with metallicity down to  $[M/H] = -3.0$ , even though the maximum is shifted inwards to higher densities. The sole exception to this trend is the  $[M/H] = +0.5$  atmosphere model in the hottest sequence presented here ( $T_{\text{eff}} = 2500\text{K}$ ), which counterintuitively shows a smaller  $J_*$  than the lower-metallicity models of that sequence. Since the gas temperature is already high in this model, not much backwarming is needed to move the model out of the temperature window of efficient nucleation (compare 1<sup>st</sup> and 2<sup>nd</sup> panel in Fig 2).

For lower metallicities ( $[M/H] < -3.0$ ), the trend of decreasing nucleation maximum with  $[M/H]$  is reversed due to the appearance of the second, inner  $J_*^{\max}$ . The reason for this is the strongly decreasing local temperature above the convection zone with decreasing metallicity, which allows a strong supersaturation (compare Sect. 4.4). The result is a growing second maximum of the nucleation rate with decreasing metallicity at the cloud base.

Our results show that dust may persist down to extremely low values of metallicity. A combination of low metallicity, high effective temperature and low surface gravity is required to prevent the formation of dust clouds. Therefore, only the  $\log(g) = 3.0$  sequence, representing the planetary atmospheres in our sample, features no dust at all for  $[M/H] < -4.0$ .

The growth velocity of the mean particle typically has two local maxima. The outer maximum of the growth velocity decreases and is shifted to higher pressures for decreasing metallicities. It vanishes as soon as the temperature inversion sets in for  $[M/H] < -4.0$ . The deeper located second maximum of the growth velocity is also shifted inwards. However, it is neither affected by the temperature inversion, nor does it decrease continuously with the metallicity, because the inward shift brings it much closer to the convection zone and therefore a more efficient element replenishment. Around  $[M/H] = -4.0$  the cloud indeed dips into the convection zone for our young giant planet-like models ( $T_{\text{eff}} = 2000\text{K}$ ,  $\log(g) = 3.0$ ), which sparks an additional growth by one order of magnitude in those models.

Due to the proximity to the convection zone and the resulting high growth velocity, the maximum mean grain radius increases slightly with decreasing metallicity down to  $[M/H] = -3.5$ . Only for lower metallicities, the decreasing abundances are finally able to cause a decreasing maximum mean grain size.

The drift velocity decreases much stronger for lower effective temperatures and to a lesser extend for higher surface gravities. As a lower drift velocity results in a stronger accumula-

tion of dust particles, the number density in the lower cloud is strongly increasing with decreasing effective temperature.

#### 4.4. The phase-non-equilibrium of the clouds

The thermodynamic conditions in an undepleted substellar atmosphere guarantee a strong supersaturation of a wide range of solid compounds. An initial high supersaturation does not automatically yield a phase equilibrium between the depleted atmosphere and the dust cloud as such (Helling, Woitke, & Thi 2008c). The phase equilibrium would require a sufficiently high number density of reactants as well as high collision and reaction rates. However, this is usually not the case for most of the solids of interest. Therefore, all three quantities need to be considered in order to avoid the overrated dust growth and gas phase depletion of the phase equilibrium approach. According to our model (see Woitke & Helling (2003); Helling & Woitke (2006)), most of the atmosphere is in phase non-equilibrium, a chemical equivalent to the NLTE state of radiation fields.

Solid grains or liquid droplets are composed of so-called monomer units. Experiments show that most of the complex monomers like  $\text{Mg}_2\text{SiO}_4$  do not exist in the gas phase (e.g. Rietmeijer et al. (1999)). The formation of such solid units would require multi body reactions which makes the probability for their formation in the gas negligibly small. On the other hand, if the reactants are physically absorbed by a preexisting surface, their limited phase space permits a much more efficient growth reaction. The reactant of the least physically absorbed amount is called the key species. Its absorption rate determines the rate of the considered chemical surface reaction and, hence, also the supersaturation ratio for each surface reaction (Helling & Woitke 2006). In order to discuss the saturation of the atmosphere, we apply the effective supersaturation ratio for each considered solid compound as defined in Helling, Woitke, & Thi (2008c).

The effective supersaturation ratios for each of the considered solid species for the three model sequences are shown in Fig. 3. For the higher metallicities, the outer atmosphere has extremely high supersaturation ratios. The ratio is increasing with the pressure, because the concentration of reactants increases with the pressure. Further inwards, the supersaturation ratio reaches a maximum where the dust growth starts to cause a strong depletion of the gas phase. Below that point, the supersaturation decreases proportionally to the dwindling element abundances. At a certain layer, each of the ratios reaches unity. In agreement with Helling, Woitke, & Thi (2008c) and Helling (2009) we find that all solids which contain high-abundant elements (Mg, Si, O, Fe) achieve phase-equilibrium in the pressure interval where the cloud has it’s maximum dust-to-gas ratio,  $\rho_d/\rho_{\text{gas}}$  (compare Figs. 3 and 5), before the supersaturation ratios drop further below unity. Solids which contain rare elements (Ti, Al) do not feature a phase-equilibrium region.

For decreasing abundances, a higher gas density is required to reach the same amount of supersaturation. However, the supersaturation becomes weaker for lower metallicities. This, superimposed with the temperature inversion zone of the low metallicity models, results in a fast drop below unity of all supersaturation ratios, which means no dust is able to form there. Fortunate for the dust cloud in the low metallicity models is the decreasing gas temperature between the inversion zone and the convection zone. Even though the element abundances are decreasing with the metallicity, the low temperatures bring about a larger concentration of reactants. Therefore, the supersatura-

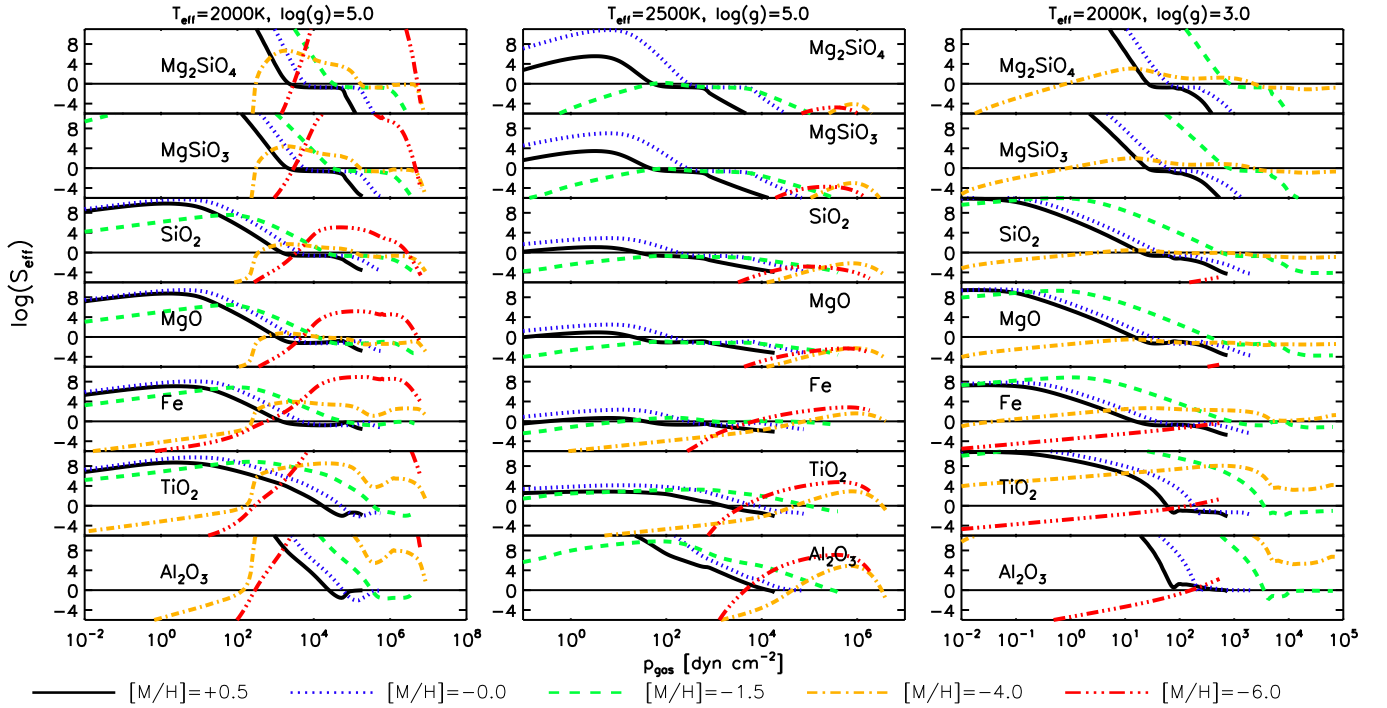


**Fig. 3.** Effective supersaturation ratio  $S_{\text{eff}}$  for three model sequences of varying metallicity  $[M/H]$ . **Left:**  $T_{\text{eff}}=2000\text{K}$ ,  $\log(g)=5.0$ ; **Center:**  $T_{\text{eff}}=2500\text{K}$ ,  $\log(g)=5.0$ , **Right:**  $T_{\text{eff}}=2000\text{K}$ ,  $\log(g)=3.0$

tion ratio in the lower atmosphere is increasing with decreasing metallicity.

In the  $[M/H]=-6.0$  model of the  $\log(g)=3.0$  sequence,  $\text{TiO}_2[\text{s}]$  is never sufficiently supersaturated for nucleation to take place. Therefore, this model is dust free.

#### 4.5. Metallicity-dependence of the cloud composition

Pure silicate dust grains are mostly transparent.  $\text{TiO}_2[\text{s}]$  and  $\text{Al}_2\text{O}_3[\text{s}]$  also do not represent strong opacities. However, even a small impurity can turn the transparency into opaqueness (Woitke 2006). This means, there is a huge difference between a mixture of pure grains and mixture of “dirty” grains. Hence, together with the grain size distribution, the composition of the mean particle is of special importance for the radiative transfer and, thus, for the spectrum.

Drift was designed to treat the formation of dirty grains. Therefore, it considers grains consisting of islands of mixed species. The composition changes with atmospheric depth and the stellar parameters. The results for the three examples sequences are shown in Fig. 4. As  $\text{TiO}_2[\text{s}]$  is the solid species which forms the dust seeds, the particles in the outer cloud are solely made of it. Ti is rare compared to the other five considered elements. Thus, as soon as growth becomes an issue, the volume fraction of  $\text{TiO}_2[\text{s}]$  decreases fast. At the higher cloud layers, where the temperatures are lower, the silicates with traces of iron dominate the dust grains. The temperatures increase with depth, eventually leading to the evaporation of the silicates, while the growth of iron becomes much more efficient, resulting in very opaque particles. Slightly deeper,  $\text{Al}_2\text{O}_3[\text{s}]$  growth dominates the volume of the average grains.

We find that the inward shift of the dust cloud yields a stronger maximum of the iron volume fraction. The opposite happens with the  $\text{Al}_2\text{O}_3[\text{s}]$  maximum, which becomes weaker.

The chemical equilibrium for the lower metallicities is changed, which leads to a significant preference of  $\text{MgO}[\text{s}]$  over the other silicates for  $[M/H] \leq -4.0$  (Fig. 4, left column). This effect is most pronounced in objects with strong dust formation and the accompanying strong gas phase depletion. For higher effective temperatures (Fig. 4, middle column), it can not be observed in our models due to the much weaker depletion, which yields a delay of the chemical equilibrium shift to even lower metallicities. In the lower temperature, low gravity sequence (Fig. 4, right column) the effect is simply not observable because no dust is present in the respective low metallicity models for the given effective temperature of 2000K. However, the changed chemical equilibrium can be observed for these low gravities as soon as the temperatures permit the formation of dust. Hence, the change from silicate to  $\text{MgO}[\text{s}]$  dominated dust grains for extremely low metallicities is observable for cooler objects. Higher surface gravities emphasize the extend of the shift.

The appearing temperature inversion zone in the low metallicity models for high gravities causes the disappearance of the wide silicate dominated cloud region, leaving an almost pure  $\text{Fe}[\text{s}]$  and  $\text{Al}_2\text{O}_3[\text{s}]$  cloud.

#### 4.6. The atmospheric dust content

The dust to gas ratio of the mass densities,  $\rho_d/\rho_{\text{gas}}$ , is a good measure for the amount of dust within the atmosphere (Fig. 5). A lower metallicity typically yields a lower  $\rho_d/\rho_{\text{gas}}$ . The exception to this is again the  $T_{\text{eff}}=2500\text{K}$   $[M/H]=+0.5$  model, because of the high temperatures (Sec. 4.3). One might assume that the dust content would scale linearly with the element abundances. However, it is not that simple, because the observed inward shift of the dust clouds with decreasing metallicity yields a higher concentration of condensable elements. This density effect partially counteracts the decreasing abundances due to decreasing metallicities. It becomes more pronounced for cooler, low grav-

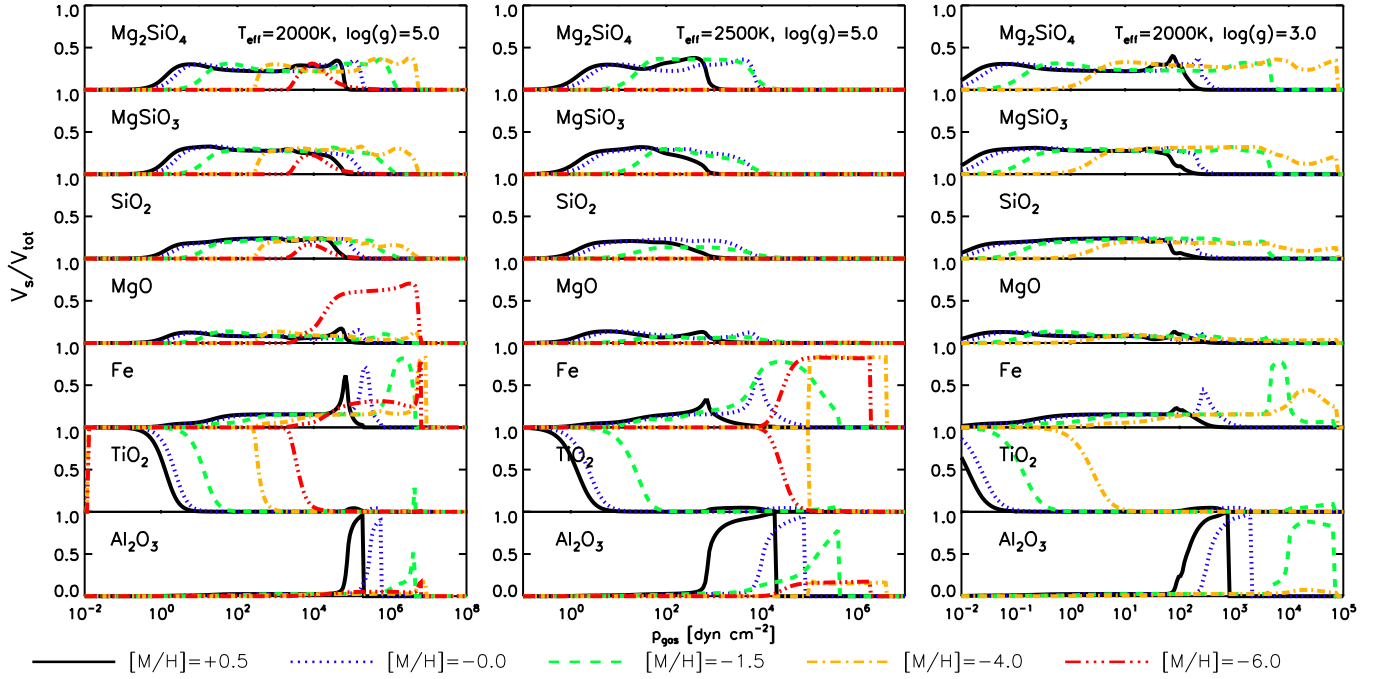


**Fig. 4.** Volume fractions,  $V_s/V_{\text{tot}}$ , for three model sequences of varying metallicity  $[M/H]$ : **Left:**  $T_{\text{eff}}=2000\text{K}$ ,  $\log(g)=5.0$ ; **Center:**  $T_{\text{eff}}=2500\text{K}$ ,  $\log(g)=5.0$ ; **Right:**  $T_{\text{eff}}=2000\text{K}$ ,  $\log(g)=3.0$

ity objects. For example, the maximum dust content decreases by merely 2.5 orders of magnitude between  $[M/H]=+0.5$  and  $[M/H]=-4.0$  in the  $T_{\text{eff}}=2000\text{K}$   $\log(g)=5.0$  sequence. Only when the cloud is not able to sink any deeper this trend ends and the dust content is finally approaching a linear scaling with the abundances.

#### 4.7. Remaining gas phase abundances

Dust formation reduces the local element abundances in the gas phase, until nucleation and growth become so weak that the depletion is fully balanced by the replenishment. At its minimum, the gas phase abundances  $\epsilon_i$  of the more rare elements can reach values below  $10^{-6}$  of their deep interior abundance  $\epsilon_{i,0}$ . Titanium is the least abundant of the six presently considered condensing elements. Especially in the outer atmosphere, which is only weakly affected by convective overshooting but its conditions allow seed formation, titanium is extremely depleted (Fig. 6).

As the efficiency of dust growth increases inwards, the depletion gets stronger. Eventually, this ends as soon as the inwards increasing element consumption by the dust formation stops to outbalance the increase of the gas density. This is due to the inwards decreasing supersaturation of the gas and the consequently less efficient growth. For supersaturation ratios below unity, the respective solids evaporate, returning their constituents to the gas phase. This enrichment can reach values of twice the deep interior model abundances.

The depletion follows the shifts of the dust cloud with the stellar parameters. There are two opposing influences on the dust growth, which cause changes in the depletion. A deeper located cloud features a more efficient growth because of the higher density. However, the inwards shift caused by a decreasing metallicity is accompanied by a decreasing growth efficiency. Hence, there is a metallicity for which the latter effect starts to cancel the former, resulting in a turn from increasing to decreasing maximum value of the relative depletion with decreasing metal-

licity. For  $T_{\text{eff}}=2000\text{K}$  and  $\log(g)=5.0$  we find this maximum depletion around  $[M/H]=-1.0$ . For higher effective temperature the turning point metallicity value is increasing, while it is decreasing for lower surface gravity.

We conclude that the strong depletion, observed in our models, can have a tremendous influence on absorption line profiles. For wavelengths at which the dust cloud is mostly transparent, one is able to see the deep and undepleted atmosphere layers. Due to their high density these layers will dominate the respective spectral lines. Because these layers are not depleted by dust formation, the full element abundances will be seen in the spectral lines. However, for the wavelengths at which the dust cloud is opaque, the observed abundances will not resemble the well-mixed interior abundances of the object. Depending on the wavelength, the observed abundances can be several orders of magnitude lower than the actual ones. Therefore, it is extremely complex to derive individual stellar abundances from spectral lines in dust-forming environments in general.

#### 4.8. Dust content and grain size above $\tau=1$

In the previous sections, the spatial distribution of dust within substellar atmospheres was analysed. It remains to be verified how much dust is observationally accessible, e.g., by polarimetry. In Fig. 7 we show the local gas pressure at the maximum of the dust-to-gas ratio  $P(\max\{\rho_d/\rho_g\})$ , the corresponding optical depth  $\tau$  and mean grain size  $\langle a \rangle$  for all three model sequences (compare to Fig. 2 and 5).

Figure 7 shows optical depth values for one single wavelength sample ( $1.2\mu\text{m}$ ;  $\tau_{1.2\mu\text{m}}$ ) and for the Planck-, Rosseland-, mean intensity- and surface-normal flux-weighted opacities ( $\tau_B$ ,  $\tau_{\text{TOSS}}$ ,  $\tau_I$  and  $\tau_F$ , respectively). At  $1.2\mu\text{m}$  the atmospheres are highly transparent. In contrast, the weighted optical depth means, in particular  $\tau_B$  which in case of the considered cool atmospheres emphasizes on the near-infrared where the dust is most opaque, are typically larger by one to two orders of magni-



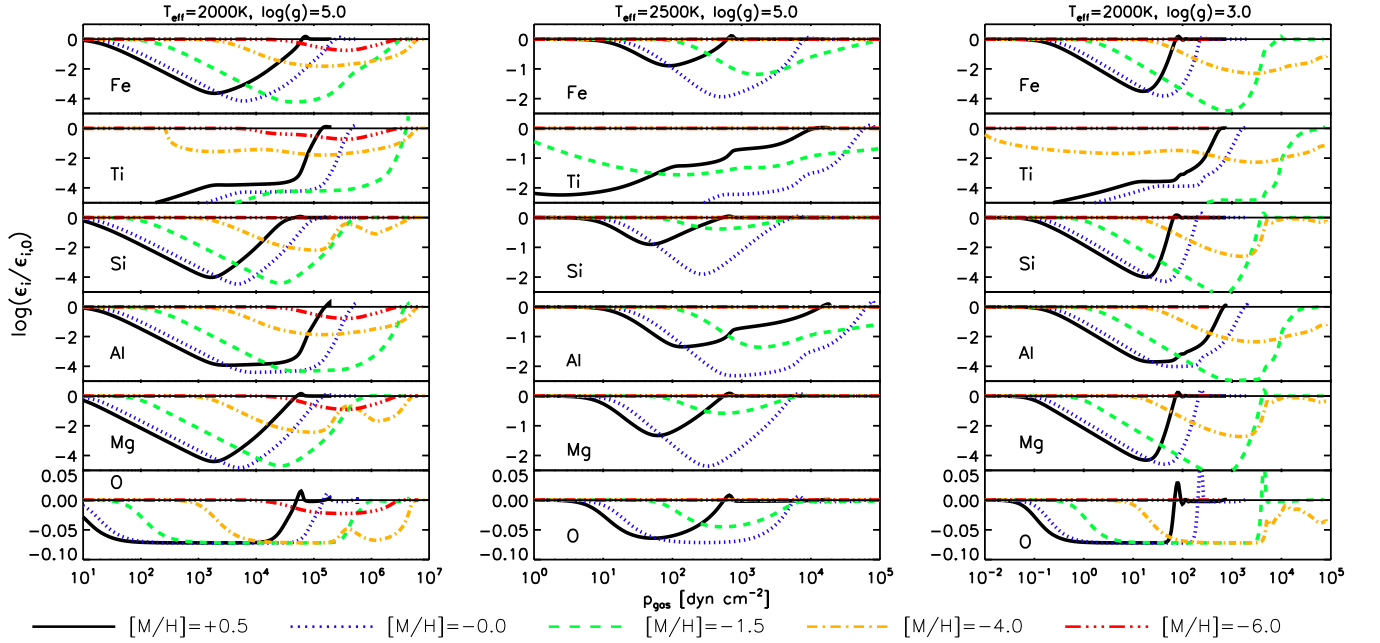


**Fig. 6.** Element abundances,  $\epsilon_i$ , for three model sequences of varying metallicity  $[M/H]$ . **Left:**  $T_{\text{eff}}=2000\text{K}$ ,  $\log(g)=5.0$ ; **Center:**  $T_{\text{eff}}=2500\text{K}$ ,  $\log(g)=5.0$ ; **Right:**  $T_{\text{eff}}=2000\text{K}$ ,  $\log(g)=3.0$

tude. The Rosseland mean is the lowest of the considered mean optical depths, as it puts emphasis on the wavelengths of lowest opacity.

The dust-to-gas ratio maximum,  $\max\{\rho_d/\rho_g\}$ , is shifted inwards for decreasing metallicities down to  $[M/H]=-3.0 \dots -4.0$ , with the exact value depending on the stellar parameters. For lower values, the  $\rho_d/\rho_g$ -maximum rises in altitude, again (Fig. 5). Therefore, all curves in Fig. 7 feature a sharp turn in local pressure around these metallicities. This clearly demonstrates the non-linear influence of the metallicity on the dust content in substellar atmospheres. Between about  $[M/H]=-0.5$  and  $+1.0$  the mean grain size and the optical depths remain more or less constant in all three model sequences, although the gas pressure changes by almost one order of magnitude. For lower  $[M/H]$  down to  $[M/H]\approx-3.5$ , the optical depths start to decrease slowly, while the size of the visible dust particles is increasing by about one half order of magnitude. This amplitude becomes stronger for closer proximities to the convection zone, which in our case concerns the low metallicity models of the  $T_{\text{eff}}=2000\text{K}$  and  $\log(g)=3.0$  sequence. In general, this means larger particles are present in the visible dense cloud layers for decreasing metallicities down to  $[M/H]\approx-3.5$ . The mean particle sizes increase up to several  $10\mu\text{m}$ , making it once more difficult to observe the major fraction of the dust in the optically thin parts of the cloud.

The outward shift of the dust-to-gas ratio maximum below  $[M/H]\approx-3.5$  amplifies the decreasing abundances, which results in a strong decline of the visible particle size, while the optical depth is continuously decreasing with the metallicity. The optical depth rise for increasing metal abundances becomes stronger for lower effective temperatures as the amount of dust becomes much larger and the dust opacity is increasingly affected by solid iron.

In order to show trends for the amount and average size of visible particles, it is best to choose a mean optical depth which focuses on those wavelengths at which the dust opacity has a strong impact, i.e., where  $\tau = 1$  is located within the cloud. From Fig. 7 one can see that  $\tau_B$  is the best applicable optical depth of our five examples. Hence, Fig. 8 depicts the dust-to-gas

ratio and mean grain size at  $\tau_B = 1$  for varied metallicities. From Fig. 7 it is obvious that the dust clouds for  $T_{\text{eff}}=2500\text{K}$  are not strongly enough developed, which is why  $\tau = 1$  is only reached below the clouds for all considered metallicities. Hence, there is neither a dust-to-gas ratio nor a grain size for  $T_{\text{eff}}=2500\text{K}$  sampled in Fig. 8. For the same reason, there are no data points for  $T_{\text{eff}}=2000\text{K}$ ,  $\log(g)=3.0$  and  $[M/H]\leq-4.0$  and the  $T_{\text{eff}}=2000\text{K}$ ,  $\log(g)=5.0$  and  $[M/H]=-6.0$  model. Both curves shown for the dust-to-gas ratio back the simple assumption that the ratio is decreasing with metallicity. However, the visible dust-to-gas ratio in both model sequences drops by merely two orders of magnitude between  $[M/H]=+1.0$  and  $[M/H]=-3.5$  (compare Sec. 4.6). This apparent discrepancy can be explained by the cooler atmospheres for lower metallicities, which enable the dust cloud to form in atmosphere layers of higher gas pressure, which involves a much more efficient dust formation. This increase in efficiency is able to slow down the decrease of the dust-to-gas ratio with the metallicity. Only for metallicities below  $[M/H]=-3.5$  the atmospheres will not become significantly cooler for lower metallicities. Thus, the cloud is no longer able to sink any deeper and the dust-to-gas ratio is finally dropping fast with metallicity, until the gas is no longer supersaturated and no dust is able to form.

In contrast to the visible dust-to-gas ratio, the mean grain size at  $\tau_B=1$  is increasing for lower metal abundances. Comparing Fig. 2 and Fig. 7 one finds that this is due to the higher gas densities at low metallicity clouds. In addition, the close proximity of the convection zone yields additional growth of the mean grain size for the  $\log(g)=3.0$  sequence, which is visible for  $[M/H]\leq-2.5$ . For a higher surface gravity ( $\log(g)=5.0$ ) this is of lesser concern, as it is only visible in the spike at  $[M/H]=-3.5$ . For lower metallicities, the dust cloud is no longer shifted to higher pressures. Therefore, the dust growth becomes purely affected by the decreasing abundance and the visible particles become smaller and smaller.

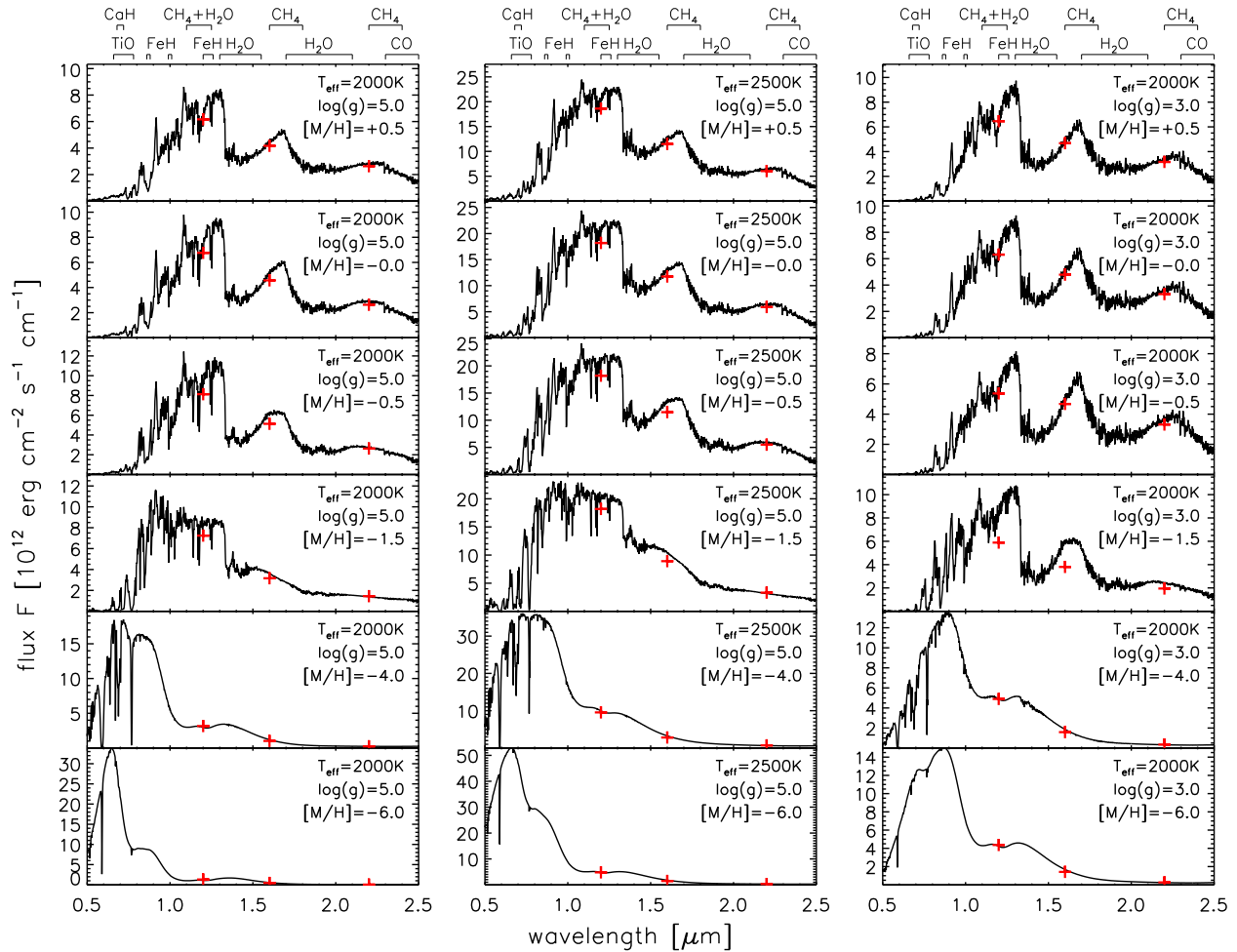


**Fig. 9.** Spectral sequences. The red crosses indicate the photometric fluxes in J, H and K bands as they would be observed by 2MASS with the respective J, H and K filters. See also Tab. 2. Note that the flux scales differ between individual plots.

## 5. Results: Spectral appearance

### 5.1. Spectral energy distribution for varied metallicities

The model spectra sequences, including additional spectra for  $[M/H]=-0.5$ , are shown in Fig. 9. For a better comparison of the shape of the spectra, they were binned to a lower resolution. For convenience, Tab. 2 contains photometric flux data for the three model sequences. We add a note of caution as these results might suggest an easy comparison with other atmosphere simulations. Helling et al. (2008a) did show that different approaches of modelling dust in substellar atmospheres can yield different results already for quantities like mean grain size and dust-to-gas ratio (see their Fig. 2) that determine the dust opacity in the radiative transfer calculations. Their comparison of synthetic colours suggests an uncertainty between 10%–30% in the 2MASS JHKs colours amongst the different atmosphere simulations.

The high metallicity models contain strong molecular absorption features. Most prominent are the water and carbon-monoxide bands between 1.0 and 3.5  $\mu\text{m}$ . For  $[M/H]=-1.5$  these bands have almost completely vanished in the high  $\log(g)$  models. In the low  $\log(g)$  models, the same happens for slightly lower metallicities. The overall spectra start become much bluer, as collision induced absorption (CIA) becomes significant. However, the dust opacity is still strong enough to conceal atmospheric regions of strong CIA and therefore compen-

sate its growing influence below 1.0  $\mu\text{m}$  and to cause a strong absorption between 1.0 and 2.0  $\mu\text{m}$ . Hence, the dust cloud delays the trend of the spectra appearing bluer. Reduction of the metal abundances starts to change this, however. In the  $[M/H]=-2.5$  models, the dust cloud has already become way too transparent in the infrared to cover the strong CIA opacity below. The impact of CIA is by orders larger than the impact of the dust. Despite that, the dust opacity is far from negligible. Especially at wavelengths shorter than 1.5  $\mu\text{m}$  the spectrum is still strongly affected by the dust. While all other opacities vanish fast with the metallicities, the alkali lines in the optical and near-infrared are getting stronger down to  $[M/H]=-4.0$ . This is because the view into deeper atmospheric layers becomes possible, where the pressure and density are higher, causing higher collision rates and thereby stronger lines (Johnas 2007). For even lower metallicities, the dust opacity vanishes and the alkali lines get weaker. The most extreme metallicity examples ( $[M/H]=-6.0$ ) are almost featureless in their spectra. The dust opacity is finally insignificant, while the spectral shape is alone determined by CIA.

Unfortunately, none of our model spectra show any significantly strong dust opacity features in the near- and mid-IR, which might provide a good tool to observationally test the dust properties other than by polarimetry (Sengupta 2008; Lecavelier Des Etangs et al. 2008).

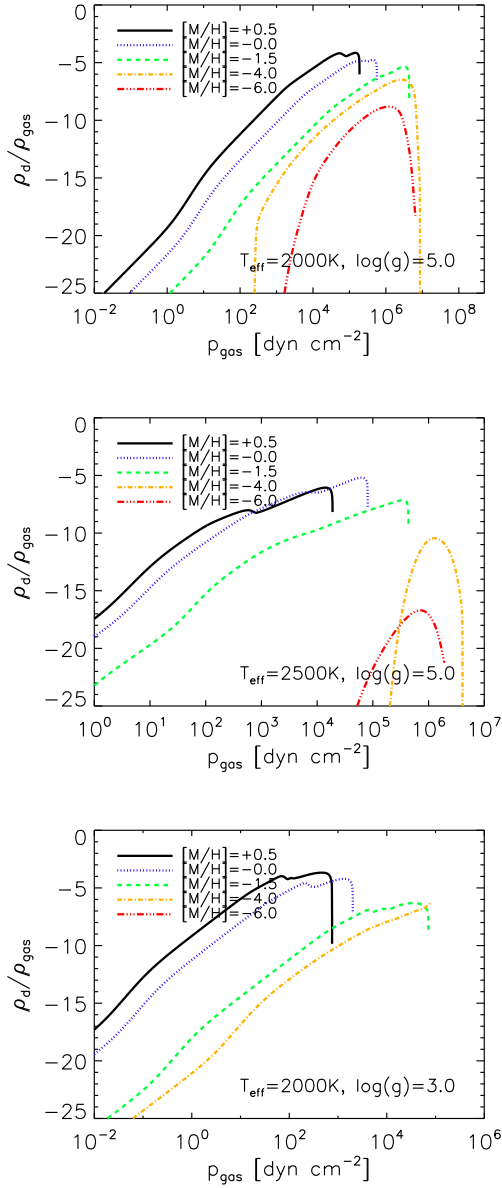


**Fig. 5.** Dust-to-gas mass ratio  $\rho_d/\rho_{gas}$ , demonstrating the dust content for three model sequences of varying metallicity  $[M/H]$ . **Top:**  $T_{eff}=2000K$ ,  $\log(g)=5.0$ ; **Center:**  $T_{eff}=2500K$ ,  $\log(g)=5.0$ ; **Bottom:**  $T_{eff}=2000K$ ,  $\log(g)=3.0$

	$[M/H]$	$\log(F)$ [ $\text{erg cm}^{-2} \text{s}^{-1} \text{Å}^{-1}$ ]								
		$T_{eff}=2000K$ , $\log(g)=5.0$			$T_{eff}=2500K$ , $\log(g)=5.0$			$T_{eff}=2000K$ , $\log(g)=3.0$		
		J	H	K	J	H	K	J	H	K
2MASS	+0.5	4.79	4.62	4.42	5.27	5.06	4.78	4.73	4.67	4.52
	-0.0	4.83	4.66	4.43	5.27	5.07	4.77	4.80	4.68	4.52
	-0.5	4.91	4.71	4.42	5.26	5.07	4.74	4.73	4.67	4.52
	-1.5	4.86	4.50	4.16	5.26	4.96	4.52	4.77	4.58	4.29
	-4.0	4.50	4.01	3.40	4.98	4.45	3.85	4.69	4.20	3.54
-6.0	4.12	3.66	2.74	4.69	4.18	3.49	4.64	4.15	3.42	
UKIRT	+0.5	4.85	4.62	4.41	5.32	5.06	4.77	4.82	4.66	4.52
	-0.0	4.90	4.66	4.42	5.32	5.07	4.76	4.88	4.68	4.52
	-0.5	5.00	4.71	4.41	5.31	5.07	4.73	4.82	4.66	4.52
	-1.5	4.91	4.51	4.14	5.29	4.97	4.50	4.86	4.58	4.28
	-4.0	4.50	4.04	3.39	4.98	4.47	3.82	4.70	4.22	3.52
-6.0	4.11	3.70	2.72	4.69	4.21	3.46	4.64	4.18	3.39	

**Table 2.** Exemplary logarithmic photometric fluxes for JHK-bands as seen by 2MASS and UKIRT.

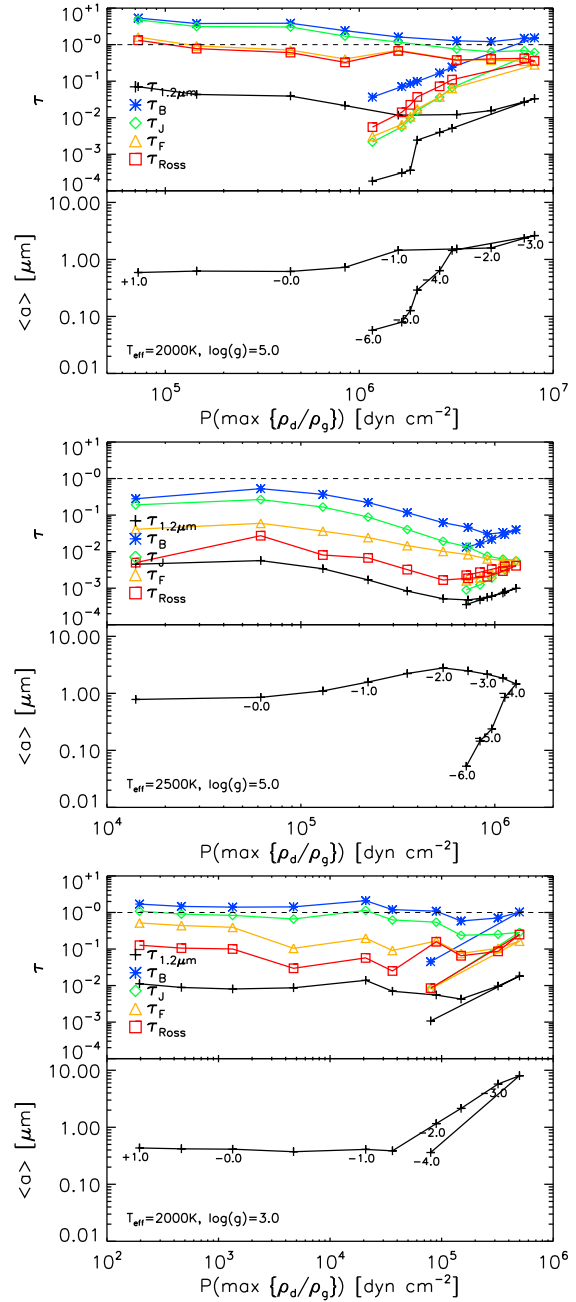


**Fig. 7.** Optical depth  $\tau$  (upper panels) and mean grain size  $\langle a \rangle$  (lower panels) at the pressure of the dust-to-gas ratio maximum  $P(\max\{\rho_d/\rho_g\})$  for varied metallicities. **Top:**  $T_{eff}=2000K$ ,  $\log(g)=5.0$ ; **Center:**  $T_{eff}=2500K$ ,  $\log(g)=5.0$ ; **Bottom:**  $T_{eff}=2000K$ ,  $\log(g)=3.0$  Five optical depths are studied: the optical depth at  $1.2\mu\text{m}$  ( $\tau_{1.2\mu\text{m}}$ ), the Planck-weighted mean ( $\tau_B$ ), weighted means for the mean intensity ( $\tau_J$ ) and surface-normal flux ( $\tau_F$ ) and the Rosseland-mean ( $\tau_{Ross}$ ). The metallicity is displayed at the respective data points.

## 5.2. Impact of varied relative abundances

Furthermore, we have studied the influence of diverging solar element abundance data sets. Our standard data set for the present model grid corresponds to the results of Grevesse et al. (1992), hereafter called *Grevesse (old)*. We compare these result to models, using the newer results by Grevesse et al. (2007), hereafter *Grevesse (new)*. The third configuration is in accordance with the

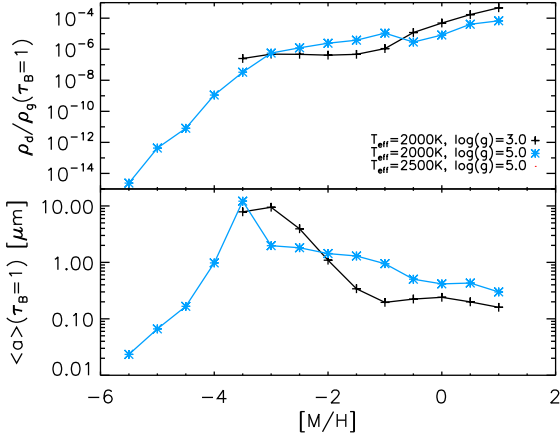


**Fig. 8.** dust-to-gas ratio (*upper panel*) and mean grain size (*lower panels*) at  $\tau_B = 1$  as a function of the metallicity. Note that the dust cloud is not optically thick for  $T_{\text{eff}}=2500\text{K}$  and, hence, is located above  $\tau_B = 1$ , which is why there are no data points for this effective temperature. For the same reason, there are no data point for  $T_{\text{eff}}=2000\text{K}$ ,  $\log(g)=3.0$  and  $[M/H] \leq -4.0$  and  $T_{\text{eff}}=2000\text{K}$ ,  $\log(g)=5.0$  and  $[M/H] \leq -6.0$ .

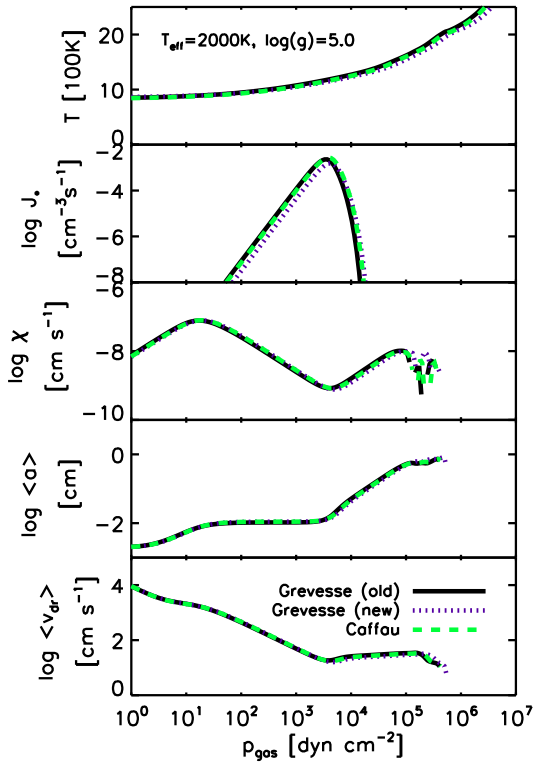


**Fig. 10.** Temperature and dust cloud structure for three different solar abundance data sets: *Grevesse (old)* corresponds to Grevesse et al. (1992), *Grevesse (new)* to Grevesse et al. (2007) and *Caffau* to the Grevesse et al. (2007) data, but using the revised O-abundance by Caffau et al. (2008)

*Grevesse (new)* models, except that we use the revised oxygen abundance determined by Caffau et al. (2008), in the following shortened to *Caffau*.

In general, the differences between our results for the three configurations remain extremely small, concerning the atmosphere and dust cloud structures. Compared to Grevesse et al.

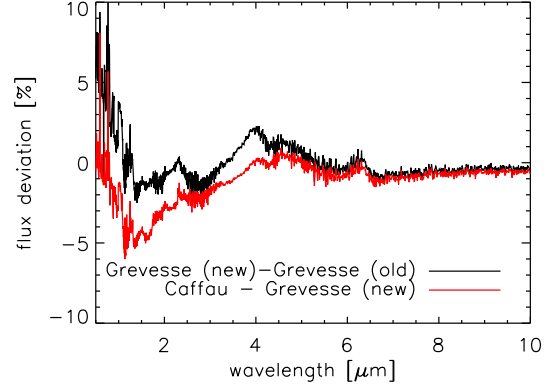


**Fig. 11.** Deviation between the respective spectra for the three considered solar abundance sets.

(1992) most element abundance values have been adjusted in Grevesse et al. (2007) (*Grevesse (new)*). However, although the physics considered for the determination the solar photospheric abundances may have been refined, their basis is quite the same. Hence, the values of both sets do not differ considerably for the majority of elements. The *Grevesse (new)* configuration contains a mostly smaller amount of the more abundant heavy elements. The consequence is a smaller gas opacity, which, in turn, results in few Kelvins cooler atmosphere, see uppermost panel Fig. 10. The oxygen abundance of *Caffau* lies in between both *Grevesse* configurations. Thus, the respective model properties are in between as well, though somewhat more resembling *Grevesse (old)* with its even higher oxygen abundance. Concerning the dust, the slightly reduced molecular abundances yield a similar result as a decrease of the metallicity, but on a much smaller scale. The whole dust cloud is marginally shifted inwards from *Grevesse (old)* over *Caffau* to *Grevesse (new)*. The resulting higher gas density at the cloud balances the reduced abundances with respect to the concentration of reactants, which contribute to the dust growth. Therefore, the mean grain sizes and number densities remain almost unaffected. The conclusion is that our integrated dust cloud / atmosphere model structures are very stable against slight abundance variations.

The corresponding spectra (Fig. 11) can differ remarkably, especially in the near-infrared. Hence, in contrast to the dust, the photometry of the models depends significantly on the abundance data set, possibly much stronger than our limited test shows. This is particularly interesting for studies on the low-metallicity class of substellar subdwarfs (Burgasser et al. 2009) as the interior element abundance pattern can deviate from the solar abundances already for moderate subsolar metallicities of  $[M/H] \lesssim -2.0$  caused by deviations in the star formation history, which has been observed in e.g., the Carina dwarf galaxy (Koch et al. 2008). A simple scaling of the element abundances might not be sufficient. The interpretation of low-metallicity substellar objects, therefore, represents a multi-fold challenge: These objects are suggested to still produce dust in their atmospheres, hence, deplete the elements in an inhomogeneous way. Additionally, the subdwarfs might exhibit a strongly non-solar element abundance pattern depending on the history of their star-formation region.

In order to estimate the influence of extreme abundance patterns like in the early universe on the atmosphere models, we have calculated such a model for  $T_{\text{eff}}=2000\text{K}$  and  $\log(g)=5.0$ , featuring an observed early universe element abundance pattern reported by Frebel et al. (2008). Therein, most heavy elements are considerably less abundant than in the solar environment. On

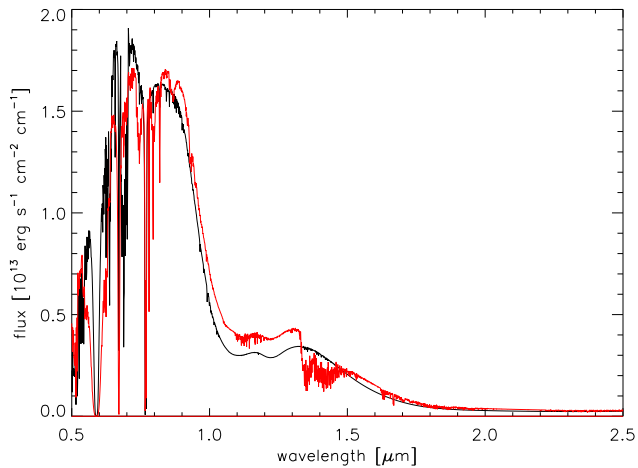


**Fig. 12.** Comparison of a standard spectrum for  $T_{\text{eff}}=2000\text{K}$ ,  $\log(g)=5.0$ ,  $[M/H]=-4.0$  (black) and a spectrum for the same effective temperature and surface gravity but applying the abundances of Frebel et al. (2008) (red).

the average, the abundances are comparable to  $[M/H]<-4.0$  for a plain scaling of the solar abundances, but the relative abundances have changed noticeably. Most important are the elements C, N and O which are highly abundant compared to higher order elements and, therefore, resemble  $[M/H]\sim-2.0$ . All this strongly influences the chemical equilibrium in the atmosphere. Especially, the carbon/oxygen ratio of the given abundance data set has changed to a degree that the chemistry is almost tipped to a carbon dominated chemistry ( $[C/O] \approx 1.0$ ). Much of the carbon is already bound in methane because of the increased gas density, freeing up a large amount of oxygen. For this reason, strong water bands are present in the near infrared (Fig. 12). The amount of dust within this atmosphere is of the same order of magnitude as we find it for  $[M/H]\approx-4.0\dots-4.5$  by simple scaling of the solar abundances. Merely, some details of the radial dust cloud structure are washed out but are still present. However, the early universe abundances feature significantly less iron. Hence, the mean opacity of the dust grains is strongly reduced as much less iron condenses. In general, the overall dust cloud characteristics as described in Sect. 4 remain.

We have shown that the dust cloud is very resistant against variations of individual abundances, while the spectra can sensitively reflect such abundance variations. That is especially true for the radical change in the relative abundances reported by Frebel et al. (2008) which reflect the influence of individual supernovae in the early universe. The richness of C, N and O yields large amounts of CO, H<sub>2</sub>O, CH<sub>4</sub> and N<sub>2</sub>. Of them, especially the H<sub>2</sub>O leaves strong marks in the near infrared at 1.15, 1.4 and 1.8 $\mu\text{m}$ . The much weaker dust opacity due to the weaker iron contribution permits a deeper view into the atmosphere which, combined with slightly higher alkali abundances, results in significantly stronger alkali lines, involving a redistribution of red optical flux into the near infrared. In addition, the deeper look into the atmosphere provides stronger TiO and FeH features shortwards of 1 $\mu\text{m}$  and slight adjustments to the near-infrared CIA opacity.

## 6. Conclusions

The results of this paper on dust formation in low metallicity substellar objects are of interest for a variety of objects or scenarios involving dust at similarly low metallicities, like for instance

star formation. Our results provide first theoretically obtained information on low-metallicity dust characteristics that determine the opacity, and we, therefore, generally conclude that

- Dust can form at very low metallicities but the dust-to-gas ratio decreases with decreasing metallicity.
- The mean grain size decrease with decreasing metallicities for a given local temperature and density leaving behind a less depleted gas phase than for higher metallicities.
- The dust material composition changes from Mg/Si-silicate-dominated to MgO/Fe-dominated with decreasing metallicity at about  $[M/H]=-4.0$ .

More specifically, our investigation suggests that dust clouds are present throughout the late M- and L-dwarf regime and into the regime of hot giant gas planets. Dust is able to form even for extremely low metal abundances. Only a combination of these low element abundances with higher effective temperatures or very low surface gravities are able to overturn the strong gas phase supersaturation and thereby dissolve the dust cloud. Therefore, only the youngest and most massive among brown dwarfs and giant gas planets could resist dust formation.

The dust clouds in our models are shifted inwards for decreasing effective temperature, increasing surface gravity and decreasing metallicity. This shift is responsible for the continuing strong presence of the clouds, as it yields a higher gas density, which is in parts able to compensate for the decreasing metal abundances with  $[M/H]$ . Therefore, the maximum dust content in our models does not linearly scale with the metallicity, but decreases slower than might be expected.

The convective overshooting becomes more efficient in hot, low-gravity objects and also with increasing element abundances. Hence, young, hot giant planets and brown dwarfs are likely to have high-altitude clouds compared to T- or Y-dwarfs where the clouds disappear below visibility. Thus, dust clouds may turn out as a good tool to distinguish planets from substellar companion by a pronounced polarisation signal in the planetary case. Indeed the haze-like high-altitude clouds of our models support the observational findings of Richardson et al. (2007) and Pont et al. (2008) which were confirmed by Lecavelier Des Etangs et al. (2008) and Sengupta (2008), based on their polarimetry studies.

The gas phase at the dust clouds is typically strongly depleted. In all three model sequences we find a metallicity value for which this depletion compared to the deep interior model abundances reaches a maximum. For higher and lower metallicities of the same sequence, the depletion is less strong. Because of the strong depletion, which is already present at the upper, optically thin cloud, it is risky to determine element abundances from absorption lines, as the visible abundances may not reflect the deep interior value.

We have observed a shift of the composition of the dust grains. The upper part of the dust cloud, which is dominated by silicates, in particular in the case of solar-like metallicities, vanishes due to a developing temperature inversion with decreasing metallicity. This becomes more severe if the surface gravity is getting stronger. While dust grains at the bottom of the dust cloud are almost fully made of Al<sub>2</sub>O<sub>3</sub>[s] for abundances around the solar value, a predominantly Fe[s] volume fraction is found in the extremely low metallicity cloud bases, i.e., for the oldest amongst the brown dwarfs. High temperatures and surface gravities amplify this change.

Dust features are presently not distinguishable in the synthetic spectra, as the dust opacity features in the near- to mid-infrared are too weak and too strongly convolved with the

spectral energy distribution of deeper atmosphere layers and molecule bands from above the dust cloud. However, the spectral dust features are extremely reliant on the lattice structure of individual dust grains. Unfortunately, no present dust model is able to properly treat this issue. Despite the lack of directly observable features, the dust clouds remain sufficiently dense to affect the near- and mid-infrared spectra even below  $[M/H]=-2.5$ . Adjustments to the code, in order to improve our fitting results, like the adaptation of a new EOS routine are almost complete. Subsequently, a new model grid will be produced and be available for public use.

*Acknowledgements.* SW would like to thank the Research Training Group 1351 of the German Research Foundation for funding. Furthermore, SW acknowledges the hospitality of St. Andrews University where large parts of this paper were written. Some of the calculations presented here were performed at the Höchstleistungs Rechenzentrum Nord (HLRN); at the Hamburger Sternwarte Apple G5 and Delta Opteron clusters financially supported by the DFG and the State of Hamburg; and at the National Energy Research Supercomputer Center (NERSC), which is supported by the Office of Science of the U.S. Department of Energy under Contract No. DE-AC03-76SF00098. We thank all these institutions for a generous allocation of computer time.

## References

- Ackerman, A. S. & Marley, M. S. 2001, *ApJ*, 556, 872  
 Allard, F. & Hauschildt, P. H. 1995, *ApJ*, 445, 433  
 Allard, F., Hauschildt, P. H., Alexander, D. R., Tamanai, A., & Schweitzer, A. 2001, *ApJ*, 556, 357  
 Baron, E., Hauschildt, P. H., Allard, F., et al. 2003, in *IAU Symposium*, Vol. 210, *Modelling of Stellar Atmospheres*, 19–+  
 Bate, M. R. 2005, *MNRAS*, 363, 363  
 Begemann, B., Dorschner, J., Henning, T., et al. 1997, *ApJ*, 476, 199  
 Boss, A. P. 2001, *ApJ*, 551, L167  
 Bruggeman, D. A. G. 1935, *Annalen der Physik*, 24, 636  
 Burgasser, A. J. 2004, *ApJ*, 614, L73  
 Burgasser, A. J., Kirkpatrick, J. D., Burrows, A., et al. 2003, *ApJ*, 592, 1186  
 Burgasser, A. J., Witte, S., Helling, Ch., & Hauschildt, P. H. 2009, *ApJ*, 697, 148  
 Burrows, A., Sudarsky, D., & Hubeny, I. 2006, *ApJ*, 650, 1140  
 Caffau, E., Ludwig, H.-G., Steffen, M., et al. 2008, *A&A*, 488, 1031  
 Campbell, S. W. & Lattanzio, J. C. 2008, *A&A*, 490, 769  
 Christlieb, N. 2006, in *Astronomical Society of the Pacific Conference Series*, Vol. 353, *Stellar Evolution at Low Metallicity: Mass Loss, Explosions, Cosmology*, ed. H. J. G. L. M. Lamers, N. Langer, T. Nugis, & K. Annuk, 271–+  
 Clark, P. C., Glover, S. C. O., & Klessen, R. S. 2008, *ApJ*, 672, 757  
 Cooper, C. S., Sudarsky, D., Milsom, J. A., Lunine, J. I., & Burrows, A. 2003, *ApJ*, 586, 1320  
 Dehn, M. 2007, PhD thesis, Universität Hamburg  
 Fortney, J. J., Marley, M. S., Saumon, D., & Lodders, K. 2008, *ApJ*, 683, 1104  
 Frebel, A., Aoki, W., Christlieb, N., et al. 2005, in *IAU Symposium*, Vol. 228, *From Lithium to Uranium: Elemental Tracers of Early Cosmic Evolution*, ed. V. Hill, P. François, & F. Primas, 207–212  
 Frebel, A., Collet, R., Eriksson, K., Christlieb, N., & Aoki, W. 2008, *ApJ*, 684, 588  
 Gail, H.-P., Keller, R., & Sedlmayr, E. 1984, *A&A*, 133, 320  
 Gizis, J. E. 1997, *AJ*, 113, 806  
 Greaves, J. S. 2005, *Astronomische Nachrichten*, 326, 1044  
 Greaves, J. S., Holland, W. S., & Pound, M. W. 2003, *MNRAS*, 346, 441  
 Grevesse, N., Asplund, M., & Sauval, A. J. 2007, *Space Science Reviews*, 130, 105  
 Grevesse, N., Noels, A., & Sauval, A. J. 1992, in *ESA Special Publication*, Vol. 348, *Coronal Streamers, Coronal Loops, and Coronal and Solar Wind Composition*, 305–308  
 Hauschildt, P. H. & Baron, E. 1999, *Journal of Computational and Applied Mathematics*, 109, 41  
 Helling, Ch. 2009, in *American Institute of Physics Conference Series*, Vol. 1094, *American Institute of Physics Conference Series*, ed. E. Stempels, 162–171  
 Helling, Ch., Ackerman, A., Allard, F., et al. 2008a, *MNRAS*, 391, 1854  
 Helling, Ch., Dehn, M., Woitke, P., & Hauschildt, P. H. 2008b, *ApJ*, 675, L105  
 Helling, Ch. & Rietmeijer, F. J. M. 2009, *International Journal of Astrobiology*, 8, 3  
 Helling, Ch. & Woitke, P. 2006, *A&A*, 455, 325  
 Helling, Ch., Woitke, P., & Thi, W.-F. 2008c, *A&A*, 485, 547  
 Jäger, C., Dorschner, J., Mutschke, H., Posch, T., & Henning, T. 2003, *A&A*, 408, 193  
 Jappsen, A.-K., Klessen, R. S., Glover, S. C. O., & MacLow, M.-M. 2009, *ApJ*, 696, 1065  
 Jeong, K. S., Chang, C., Sedlmayr, E., & Sülzle, D. 2000, *J.Phys.B.*, 33, 3417  
 Johnas, C. M. S. 2007, PhD thesis, Universität Hamburg  
 Jones, H. R. A. & Tsuji, T. 1997, *ApJ*, 480, L39+  
 Koch, A., Grebel, E. K., Gilmore, G. F., et al. 2008, *AJ*, 135, 1580  
 Korhonen, H., Napari, I., Timmreck, C., et al. 2003, *Journal of Geophysical Research - Atmospheres*, 108, 4546  
 Lecavelier Des Etangs, A., Pont, F., Vidal-Madjar, A., & Sing, D. 2008, *A&A*, 481, L83  
 Ledieu, J., Hoefft, J. T., Reid, D. E., et al. 2005, *Phys.Rev. B*, 72, 035420  
 Lépine, S., Rich, R. M., & Shara, M. M. 2007, *ApJ*, 669, 1235  
 Levin, Z., Ganor, E., & Gladstein, V. 1996, *J. Appl. Meteor.*, 35, 1511  
 Ludwig, H.-G., Allard, F., & Hauschildt, P. H. 2002, *A&A*, 395, 99  
 Ludwig, H.-G., Allard, F., & Hauschildt, P. H. 2006, *A&A*, 459, 599  
 Luhman, K. L., Adame, L., D’Alessio, P., et al. 2005, *ApJ*, 635, L93  
 Lunine, J. I., Hubbard, W. B., & Marley, M. 1986, *ApJ*, 310, 238  
 Mie, G. 1908, *Annalen der Physik*, 25, 377  
 Nakajima, T., Oppenheimer, B. R., Kulkarni, S. R., et al. 1995, *Nature*, 378, 463  
 Natta, A., Testi, L., Comerón, F., et al. 2002, *A&A*, 393, 597  
 Noll, K. S., Geballe, T. R., & Marley, M. S. 1997, *ApJ*, 489, L87+  
 Nuth, III, J. A. & Ferguson, F. T. 2006, *ApJ*, 649, 1178  
 Omukai, K. 2008, in *American Institute of Physics Conference Series*, Vol. 990, *First Stars III*, ed. B. W. O’Shea & A. Heger, 63–67  
 Oppenheimer, B. R., Kulkarni, S. R., Matthews, K., & van Kerkwijk, M. H. 1998, *ApJ*, 502, 932  
 Palik, E. D. 1985, *Handbook of optical constants of solids (Academic Press Handbook Series, New York: Academic Press, 1985, edited by Palik, Edward D.)*  
 Palik, E. D. 1991, *Handbook of optical constants of solids II (Boston: Academic Press, 1991, edited by Palik, Edward D.)*  
 Pont, F., Knutson, H., Gilliland, R. L., Moutou, C., & Charbonneau, D. 2008, *MNRAS*, 385, 109  
 Posch, T. 2008, private communication by Woitke & Helling (2004)  
 Rebolo, R., Zapatero-Osorio, M. R., & Martin, E. L. 1995, *Nature*, 377, 129  
 Richardson, L. J., Deming, D., Horning, K., Seager, S., & Harrington, J. 2007, *Nature*, 445, 892  
 Rietmeijer, F. J. M., Nuth, III, J. A., & Karner, J. M. 1999, *ApJ*, 527, 395  
 Scholz, A. & Jayawardhana, R. 2008, *ApJ*, 672, L49  
 Sengupta, S. 2008, *ApJ*, 683, L195  
 Sharp, C. M. & Huebner, W. F. 1990, *ApJS*, 72, 417  
 Smith, B. D. & Sigurdsson, S. 2007, *ApJ*, 661, L5  
 Tsuji, T., Ohnaka, K., & Aoki, W. 1996a, *A&A*, 305, L1+  
 Tsuji, T., Ohnaka, K., Aoki, W., & Nakajima, T. 1996b, *A&A*, 308, L29  
 Whitworth, A. P. & Stamatellos, D. 2006, *A&A*, 458, 817  
 Woitke, P. 2006, *A&A*, 460, L9  
 Woitke, P. & Helling, Ch. 2003, *A&A*, 399, 297  
 Woitke, P. & Helling, Ch. 2004, *A&A*, 414, 335  
 Wolf, S. & Voshchinnikov, N. V. 2004, *Computer Physics Communications*, 162, 113